ELSEVIER

www.elsevier.nl/locate/ica

Inorganica Chimica Acta 294 (1999) 140–152

Inorganica Chimica Acta

The relationship between surface derivatization and the physical properties of bisarylphosphinidenetriironnonacarbonyl clusters

Joanna L. Perkinson, Mu-Hyun Baik, Geoffrey E. Trullinger, Cynthia K. Schauer *, Peter S. White

Department of Chemistry, University of North Carolina, Chapel Hill, NC 27599-3290, USA

Received 3 May 1999; accepted 23 June 1999

Dedicated to Du Shriver on the occasion of his 65th birthday.

Abstract

A series of clusters, $Fe_3(CO)_9(\mu_3\text{-}P\text{–}p\text{-}C_6H_4X)(\mu_3\text{-}P\text{–}p\text{-}C_6H_4X')$ ($X = X' = NMe_2$, OCH_3, CH_3, Cl, CF_3, CN; $X = CN$, $X' = NMe_2$) has been prepared using functionalized $p\text{-}XC_6H_4PCl_2$ starting materials. The influence of changes in the X groups on the physical properties of the $Fe_3(CO)_9$ cluster core are examined. This cluster series displays two one-electron reductions to produce stable radical monoanions and diamagnetic dianions, allowing the behavior of all three species to be examined. Infrared, ^{31}P and ^{1}H NMR, and electron paramagnetic resonance (of the radical monoanion) spectroscopies as well as the structural characterization of two members of the series, $Fe_3(CO)_9(\mu_3\text{-}P\text{–}p\text{-}C_6H_4X)(\mu_3\text{-}P\text{–}p\text{-}C_6H_4X')$ ($X = X' = NMe_2$; $X = CN$, $X' = NMe_2$) by single crystal X-ray diffraction methods all indicate that the cluster structures are invariant with the nature of X. The Hammett linear free energy relationship is used to quantify the observed changes in cluster properties. Analysis of infrared, electron paramagnetic resonance and cyclic voltammetry data by the Hammett equation quantify the communication between the cluster surface and the $Fe_3(CO)_9$ core. Fenske–Hall molecular orbital calculations were used to assess the important orbital interactions between the substituted phenyl rings and the $Fe_3(CO)_9$ cluster core.

Keywords: Crystal structures; Electrochemistry; Iron complexes; Carbonyl complexes; Cluster complexes

1. Introduction

Derivatization of ligands that cap the surface of a transition metal cluster will influence the electronic properties of the metal core. These effects should be the most pronounced for small metal clusters in which the ratio of capping ligands to metal atoms is large. The triiron cluster $Fe_3(CO)_9(\mu_3\text{-}P\text{–}p\text{-}C_6H_4X)_2$, with two triply bridging arylphosphinidene ligands, provides a synthetically accessible system to study the changes in the electronic properties of the Fe_3P_2-core induced by substituting electron-withdrawing and electron-donating groups on the aryl ring appended to phosphorus. The electronic effects attendant upon substituting an aromatic ring are well-described by Hammett parameters [1]. The Fe_3P_2 system is of particular interest in context of our efforts to prepare and characterize linear arrays of transition metal clusters [2]. A variety of physical techniques are available in this system to characterize the changes at the cluster core induced by the remote aryl substituent. Infrared CO stretching frequencies directly monitor electron density changes at the $Fe_3(CO)_9$ core. The $Fe_3(CO)_9(\mu_3\text{-}P\text{–}p\text{-}C_6H_4X)_2$ clusters undergo two one-electron reductions, and changes in the reduction potentials as a function of surface derivatization are measured by cyclic voltammetry. In addition, the properties of the derivatized monoanion radicals can be monitored by electron paramagnetic resonance spectroscopy. The specific orbital interactions that communicate the electronic effect of the X substituent to the Fe_3P_2 core are identified by Fenske–Hall molecular orbital calculations. Correlations of both experimental data and results of theoretical calcu-

* Corresponding author. Tel.: +1-919-962 0808; fax: +1-919-962 2388.

0020-1693/99/$ - see front matter
PII: S0020-1693(99)00246-7

lations by the Hammett linear free energy relationship (LFER) quantify the communication between the cluster surface and $Fe_3(CO)_9$ core.

2. Results and discussion

2.1. Synthesis and characterization of the $Fe_3(CO)_9(\mu_3\text{-}P\text{–}p\text{-}C_6H_4X)(\mu_3\text{-}P\text{–}p\text{-}C_6H_4X')$ clusters

There are many reported methods to synthesize the $Fe_3(CO)_9(\mu_3\text{-}PC_6H_5)_2$ parent cluster [3]. The route developed by Muetterties and Day [4] (Eq. (1)) involving the reaction of an aryl dichlorophosphine with disodiumdiironoctacarbonyl has proven to be tolerant of the *para*-functionalized aryldichlorophosphines and allows convenient synthesis of the unsymmetrically substituted cluster by using a mixture of two aryldichlorophosphines.

$$Na_2[Fe_2(CO)_8] + (p\text{-}C_6H_4X)PCl_2 \rightarrow Fe_3(CO)_9(\mu_3\text{-}P\text{–}p\text{-}C_6H_4X)_2 \quad (1)$$

Employing this route, six symmetrically substituted clusters (X = X′; **1**–**X**) and one unsymmetrically substituted cluster (X ≠ X′; **2**–X:X′) have been synthesized (Table 1). The one unsymmetrical cluster prepared, **2**–NMe_2:CN, has the most electron-withdrawing (CN) and the most electron-donating (NMe_2) substituents studied to maximize any effects due to unsymmetrical substitution. In the reaction to prepare **2**–NMe_2:CN, all three of the expected products (**1**–CN, **1**–NMe_2, and **2**–NMe_2:CN) are observed, but the mixture can be separated readily by chromatography. Although the mechanism of the reaction between $Na_2[Fe_2(CO)_8]$ and $(p\text{-}XC_6H_4)PCl_2$ is complex, it is noteworthy that the cluster yield is highly dependent on the electronic nature of the substituent (Table 1). The clusters with electron-withdrawing substituents on the aryl group are formed in yields below 5%, while the cluster functionalized with highly electron-donating NMe_2 groups is formed in 45% yield. The basis for this difference in yield may be undesired side reactions occurring between the more oxidizing phosphines and the highly reducing $Na_2[Fe_2(CO)_8]$.

Table 1
Numbering scheme and yields of the syntheses for $Fe_3(CO)_9(\mu_3\text{-}P\text{–}p\text{-}C_6H_4X)(\mu_3\text{-}P\text{–}p\text{-}C_6H_4X')$ clusters

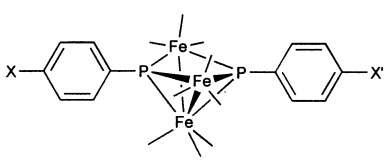

X	X′	Abbreviation for cluster	Yield (%)
NMe_2	CN	**2**–NMe_2:CN	3
NMe_2	NMe_2	**1**–NMe_2	45
OCH_3	OCH_3	**1**–OCH_3	24
CH_3	CH_3	**1**–CH_3	17
H	H	**1**–H	
Cl	Cl	**1**–Cl	4
CF_3	CF_3	**1**–CF_3	5
CN	CN	**1**–CN	10

One of the most noticeable effects of surface derivatization in this cluster series is the change in color with the electronic nature of the substituent. The cluster with the most electron-donating substituent, **1**–NMe_2, is a dark purple in color, while **1**–CF_3 is orange in color. Unfortunately, the electronic transitions in the visible region are so broad that distinct spectral features attributable to the difference in color are not discernible. Surface derivatization also has a marked effect on the solubilities of the clusters. In hexanes, **1**–CN and **1**–NMe_2 are completely insoluble, while the unsymmetrical cluster, **2**–NMe_2:CN, is moderately soluble and all of the other clusters are very soluble. All derivatized clusters are quite soluble in more polar organic solvents such as THF, Et_2O and CH_2Cl_2.

Two derivatized clusters, **2**–NMe_2:CN and **1**–NMe_2, were structurally characterized (Fig. 1). The Fe_3P_2 cluster framework is square pyramidal, with the base consisting of the two phosphorus atoms and the two irons on the non-bonding edge with an apical $Fe(CO)_3$ group. The $Fe_3(CO)_9$ cluster core has C_s symmetry, with the plane of symmetry containing the two phosphorus atoms and apical iron. Comparison of selected bond angles and distances from the two crystal structures and those of the parent cluster **1**–H (Table 2) [5] shows that no significant changes in the bonding of the phosphinidene ligand to the cluster framework occur due to surface derivatization.

The pattern of infrared CO stretches observed for all derivatized clusters is identical to that observed for the parent cluster, **1**–H. The change in frequency spanned from the most electron-donating group (NMe_2) to the most electron-withdrawing group (CN) is approximately 20 cm^{-1}. Nine infrared-active CO stretches are predicted (six symmetric and three antisymmetric). The number of bands resolved is dependent on the solvent. In a noninteracting solvent such as hexanes, eight distinct bands are observed. More polar solvents, such as Et_2O, CH_2Cl_2, THF (Table 3) only allow resolution of five, four or three bands, respectively.

The $^{31}P\{^1H\}$ NMR data for the derivatized clusters are summarized in Table 4. A singlet is observed for each symmetrically substituted cluster near 320 ppm. A small range of ^{31}P chemical shifts (12 ppm) is observed. The unsymmetrical **2**–NMe_2:CN shows the expected AB pattern ($\delta_A = 321$ ppm, $\delta_B = 309$ ppm, $^2J_{PP} = 284$ Hz). The resonances for the phosphorus nuclei bound to the CN and the NMe_2 substituted rings occur ap-

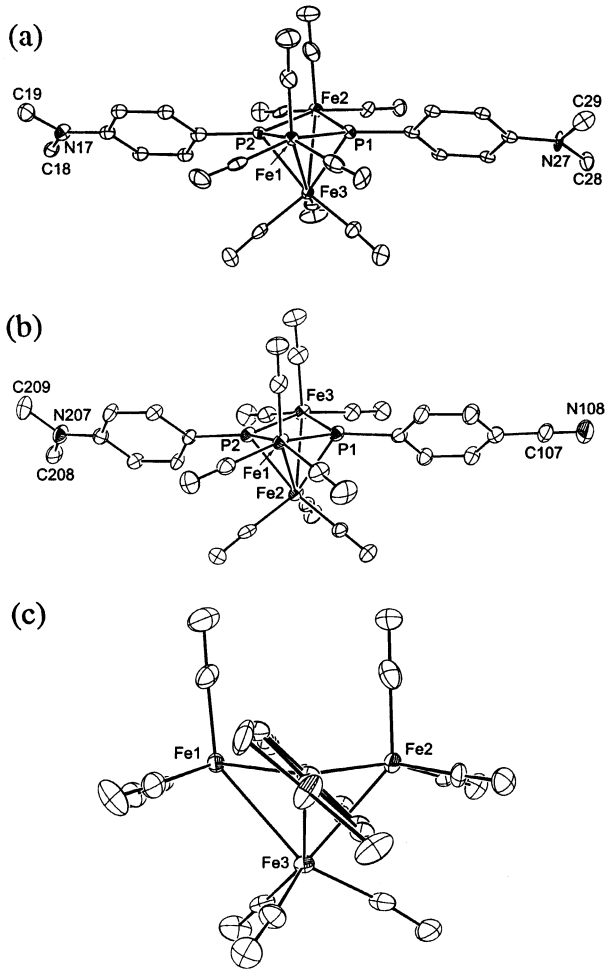

Fig. 1. (a) ORTEP diagram of $Fe_3(CO)_9[\mu_3\text{-P}–p\text{-}C_6H_4N(CH_3)_2]_2$ with ellipsoids at 50% probability level. (b) ORTEP diagram of $Fe_3(CO)_9[\mu_3\text{-P}–p\text{-}C_6H_4N(CH_3)_2][\mu_3\text{-P}–p\text{-}C_6H_4CN]\cdot C_6H_6$ with ellipsoids at 25% probability level. (c) ORTEP diagram of $Fe_3(CO)_9[\mu_3\text{-P}–p\text{-}C_6H_4N(CH_3)_2]_2$ with view along the P–P axis.

proximately at the same chemical shift as the respective symmetric clusters. The $^2J_{PP}$ value falls within the range of 200–350 Hz observed previously for bicapped triiron phosphinidene clusters with two different substituents [6]. The ^{1}H NMR data for the substituted aryl rings are summarized in Table 5. The resonances for the aryl ring protons in the derivatized clusters differ by less than 0.3 ppm from the resonances for the corresponding *para*-

Table 2
Comparison of cluster structural parameters [a]

Cluster	**1**–H [b]	**1**–NMe_2	**2**–NMe_2:CN
Fe···Fe	3.54(1)	3.545(3)	3.554(2)
Fe–Fe (avg.)	2.717(3)	2.714(2)	2.714(2)
Fe–P (avg.)	2.213(5)	2.223(2)	2.220(2); NMe_2 2.217(2); CN

[a] Distances in Å.
[b] Data from Ref. [5].

Table 3
Infrared CO stretching frequencies (cm^{-1}) of $Fe_3(CO)_9(\mu_3\text{-P}–p\text{-}C_6H_4X)_2$ in THF solution

Cluster	ν(CO)1	ν(CO)2	ν(CO)3
2–NMe_2:CN	2039 (vs)	2018 (s)	2001 (m)
1–NMe_2	2033 (vs)	2012 (s)	1994 (m)
1–OCH_3	2038 (vs)	2016 (s)	2000 (m)
1–CH_3	2040 (vs)	2018 (s)	2001 (m)
1–H	2041 (vs)	2019 (s)	2003 (m)
1–Cl	2043 (vs)	2021 (s)	2004 (m)
1–CF_3	2046 (vs)	2024 (s)	2007 (m)
1–CN	2047 (vs)	2024 (s)	2003 (m)

Table 4
The $^{31}P\{^1H\}$ NMR chemical shifts of the neutral cluster, $Fe_3(CO)_9(\mu_3\text{-P}–p\text{-}C_6H_4X)(\mu_3\text{-P}–p\text{-}C_6H_4X')$ [a], and the dianionic cluster series $Na_2[Fe_3(CO)_9(\mu_3\text{-P}–p\text{-}C_6H_4X)(\mu_3\text{-P}–p\text{-}C_6H_4X')]$ [b]

Charge	0	−2
2–NMe_2:CN [c]	321, 309, dd	31, s; 32, s
1–NMe_2	323, s	33, s
1–OCH_3	322, s	35, s
1–CH_3	323, s	37, s
1–H	320, s	35, s
1–Cl	309, s	30, s
1–CF_3	312, s	31, s
1–CN [d]	310, s	

[a] Chemical shifts, δ, are recorded in ppm as 0.01 M THF solutions at 25°C.
[b] Chemical shifts, δ, are recorded in ppm in THF at 25°C as the $[Na^+]_2$ salt.
[c] $^2J_{PP} = 280$ Hz.
[d] The dianion of **1**–CN is not observed spectroscopically.

Table 5
^{1}H NMR data for $Fe_3(CO)_9(\mu_3\text{-P}–p\text{-}C_6H_4X)(\mu_3\text{-P}–p\text{-}C_6H_4X')$ clusters [a]

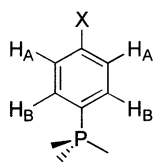

X	H_A	H_B	H [b]
1–NMe_2	6.8, d, 2H	7.6, m, 2H	3.1, s, 6H
1–OCH_3	7.0, d, 2H	7.6, m, 2H	3.8, s, 3H
1–CH_3	7.3, d, 2H	7.6, m, 2H	2.4, s, 3H
1–H	7.2, d, 2H	7.7, m, 2H	
1–Cl	7.5, d, 2H	7.7, m, 2H	
1–CF_3	7.7, d, 2H	8.2, m, 2H	
1–CN	7.8, d, 2H	8.0, m, 2H	
2–N(Me)2:CN	6.7, d, 2H [c]	7.7, m, 2H [c]	3.1, s, 6H
	7.7, d, 2H [d]	7.9, m, 2H [d]	

[a] All spectra are recorded in CD_2Cl_2 at 25°C. All chemical shifts, δ, are reported in ppm.
[b] Methyl protons.
[c] $N(Me)_2$ substituted phenyl ring.
[d] CN substituted phenyl ring.

Table 6
Infrared CO stretching frequencies (cm^{-1}) of $Na_2[Fe_3(CO)_9(\mu_3\text{-}P\text{–}p\text{-}C_6H_4X)_2]$ in THF solution

Cluster	ν(CO)1	ν(CO)2	ν(CO)3	ν(CO)4	ν(CO)5	ν(CO)6
$[\mathbf{2}\text{–}NMe_2\text{:}CN]^{2-}$	1997 (m)	1946 (s)	1918 (s)	1870 (m)	1817 (m)	1781 (m)
$[\mathbf{1}\text{–}NMe_2]^{2-}$	1992 (m)	1942 (s)	1913 (s)	1866 (m)	1811 (m)	1777 (m)
$[\mathbf{1}\text{–}OCH_3]^{2-}$	1994 (m)	1945 (s)	1917 (s)	1869 (m)	1815 (m)	1779 (m)
$[\mathbf{1}\text{–}CH_3]^{2-}$	1996 (m)	1945 (s)	1917 (s)	1871 (m)	1815 (m)	1780 (m)
$[\mathbf{1}\text{–}H]^{2-}$	1998 (m)	1948 (s)	1919 (s)	1872 (m)	1817 (m)	1783 (m)
$[\mathbf{1}\text{–}Cl]^{2-}$	1999 (m)	1949 (s)	1920 (s)	1874 (m)	1819 (m)	1784 (m)
$[\mathbf{1}\text{–}CF_3]^{2-}$	1990 (m)	1943 (s)	1922 (s)	1879 (m)	1822 (m)	1788 (m)

substituted aryldichlorophosphine. For the unsymmetric $\mathbf{2}\text{–}NMe_2$:CN, distinct resonances are observed for the two different aromatic rings.

2.2. Preparation and characterization of cluster anions

The parent cluster $\mathbf{1}\text{–}H$ can be reduced chemically to a monoanion radical and a diamagnetic dianion species (Eq. (2)). Spectroscopic characterization of these reduced clusters has been reported [3].

$$\mathbf{1}\text{–}H \rightarrow [\mathbf{1}\text{–}H]^- \rightarrow [\mathbf{1}\text{–}H]^{2-} \quad (2)$$

All derivatized clusters can likewise be reduced by one or two electrons with the exception of $\mathbf{1}\text{–}CN$, which forms a stable monoanion radical but decomposes upon addition of a second reducing equivalent. Unlike the neutral clusters, it has not been possible to obtain crystals of the monoanion or dianion complexes; however, spectroscopic characterization of these species indicates that the structures of the monoanion and dianion clusters are not affected by the aryl ring substituents.

The pattern of carbonyl stretches observed for the derivatized monoanion radicals, $[\mathbf{1}\text{–}X]^-$ and $[\mathbf{2}\text{–}NMe_2\text{:}CN]^-$, is identical to $[\mathbf{1}\text{–}H]^-$. The fact that the IR pattern is consistent through the series indicates that the cluster structure is unchanged by varying X. The changes between the spectra of the neutral, mono-, and dianionic clusters suggest that structural changes occur upon reduction of the cluster.

Electron paramagnetic resonance (EPR) spectroscopy has been utilized also to characterize the derivatized radical anions. Hyperfine interaction of the unpaired electron with the two $I = 1/2$ ^{31}P nuclei can provide information about the structure of the monoanion. Similarly to $[\mathbf{1}\text{–}H]^-$, the EPR spectrum for each species is a triplet (Fig. 2), indicating that the unpaired electron is coupling to two magnetically equivalent phosphorus nuclei. The observed g values do not vary substantially as a function of X. As is typical for metal carbonyl compounds, the g values are close to the free electron value of 2.0023, indicating that the singly occupied orbital is delocalized and largely metal in character [7]. The hyperfine coupling constant for the series is invariant at 12 Gauss within the ± 1 Gauss experimental error.

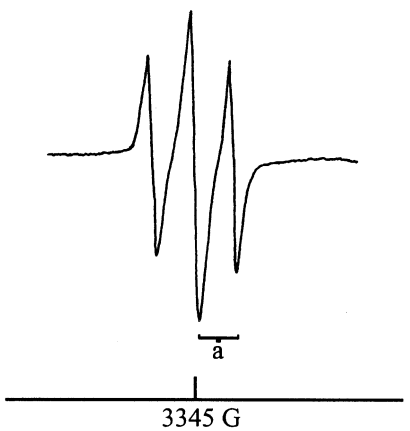

Fig. 2. EPR spectrum of $Na[Fe_3(CO)_9(\mu_3\text{-}P\text{–}p\text{-}C_6H_4CF_3)_2]$ in THF solution at room temperature, $< a >_p = 13$ Gauss.

The pattern of CO stretches for the dianion clusters $[\mathbf{1}\text{–}X]^{2-}$ and $[\mathbf{2}\text{–}NMe_2\text{:}CN]^{2-}$, is also identical to $[\mathbf{1}\text{–}H]^{2-}$ (Table 6). The observed pattern is considerably different than for the monoanion, with the two most intense bands of the dianion lying approximately 45 cm^{-1} lower in energy than the two comparable bands of the monoanion. The ^{31}P NMR resonance for $[\mathbf{1}\text{–}H]^{2-}$ and the derivatized dianions is observed at approximately 35 ppm (Table 4)[1] which is not in the 275–480 ppm range expected for an alkyl or aryl substituted phosphinidene phosphorus nucleus [3]. A singlet is observed for each of the symmetric clusters and the unsymmetrically substituted cluster exhibits two singlets separated by 1 ppm. The range of resonances from the most electron-withdrawing to the most electron-donating is approximately 10 ppm (Table 4).

The reduction of the neutral clusters to the radical monoanion and dianion can be observed in a cyclic voltammetry experiment. The cyclic voltammogram of $\mathbf{1}\text{–}CF_3$ is presented in Fig. 3 as a representative exam-

[1] The most likely explanation for this unusual chemical shift is a rearrangement of the Fe–P bonding upon reduction.

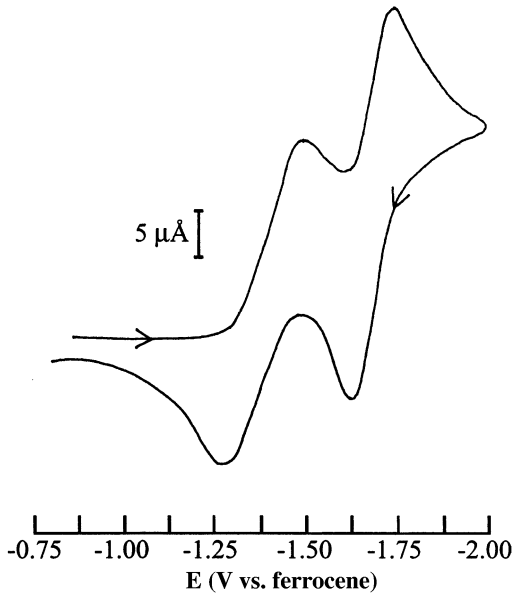

Fig. 3. Cyclic voltammogram of a 1 mM solution of **1**–CF_3 in 0.1 M of $(NBu_4)[PF_6]$/THF (Pt working electrode, scan rate = 50 mV s^{-1}).

ple for the cluster series. The functionalized clusters all exhibit two one-electron reduction waves (Table 7). The variation in the ΔE_p values with scan rate demonstrate that the observed waves of each clusters are only electrochemically quasi-reversible. As expected, the clusters with electron-withdrawing substituents are reduced at more positive potentials than cluster with electron-donating substituents. The potential spanned for the first reduction values for the derivatized clusters is approximately 330 mV while that for the second reduction is 170 mV. It is not clear why the second reduction potential range is smaller than the first. To place these results in context, direct substitution at the iron core in the cluster series, $Fe_3(CO)_{9-x}(L)_x(\mu_3\text{-}PC_6H_5)_2$ (L = $P(OMe)_3$, PEt_3), results in a shift of $E_{1/2}$ by 250 mV to more negative potentials with each sequential substitution of a CO ligand by an L group [8].

2.3. Correlation of cluster spectroscopic data with the Hammett equation

Correlations of the observed spectroscopic parameters for the clusters derivatized with substituted aryl rings can be examined by the Hammett linear free energy relationship [1]. The Hammett σ parameter is a constant whose value depends only on the electronic nature of the substituent and the position on the aromatic ring. For the Hammett σ parameters to be applied to a series, the detector region (the cluster in this case) must remain structurally constant and the source (the substituted aryl ring) must be far enough removed from the detector site so that the induced changes in the molecular orbitals of the detector region remain small. The structural similarity of the $Fe_3(CO)_9$ core within the cluster series has been determined by single crystal X-ray structural analysis for the neutral series, and that of the anions has been deduced by spectroscopic means. Correlations are examined below between the Hammett σ parameter and IR data, EPR data, and cyclic voltammetry data, each of which qualitatively reflects electronic density changes occurring at the core. NMR chemical shifts were also examined, but no correlation with the Hammett parameters is seen. Results of Fenske–Hall molecular orbital calculations are also presented, which provide a description of the electron distribution in the clusters and allow determination of the important orbital interactions between the aryl ring and the cluster core.

2.3.1. Infrared data

Infrared carbonyl stretching frequencies are very sensitive to electron density on the metal, due to the σ donor and π acceptor nature of the bonding between transition metals and carbonyl ligands. Increasing the electron density in the π* orbitals of the CO ligands lowers the CO stretching frequency, which is observed in infrared spectroscopy. For the $Fe_3(CO)_9(\mu_3\text{-P–}p\text{-}$

Table 7
Electrochemical data for $Fe_3(CO)_9(\mu_3\text{-P–}p\text{-}C_6H_4X)(\mu_3\text{-P–}p\text{-}C_6H_4X')$ [a]

Cluster	$E^1_{1/2}$ (V)	$E^2_{1/2}$ (V)	ΔE^1_p (mV)	ΔE^2_p (mV)	i_{pa}/i_{pc}
2–NMe_2:CN	−1.47	−1.76	210	120	0.79
1–NMe_2	−1.63	−1.79	100	80	0.91
1–OCH_3	−1.53	−1.76	170	110	0.82
1–CH_3	−1.46	−1.74	210	117	0.75
1–H	−1.47	−1.72	180	130	0.95
1–Cl	−1.35	−1.70	220	120	0.82
1–CF_3	−1.34	−1.67	190	100	0.93
1–CN	−1.30	−1.63	230	140	0.84

[a] $E_{1/2}$ values are recorded at 50 mV s^{-1} scan rate as 1 mM solutions of cluster and 0.1 M solutions of $(n\text{-}Bu_4N)[PF_6]$ in THF. These values are recorded with $E_{1/2}$ of an internal ferrocene standard at 0 V. ΔE_p values are determined using an internal ferrocene standard.

$C_6H_4X)(\mu_3\text{-P}–p\text{-}C_6H_4X')$ cluster series, it is expected that electron-donating groups will lower the CO stretching frequencies and electron-withdrawing groups will have the opposite effect. A correlation between the CO stretching frequencies and the Hammett parameters is theoretically justified only if the observed vibrational frequencies reflect the CO stretching force constant [9].

A plot of ν(CO) for the most intense band of the neutral cluster versus σ_p gives a positive slope with a good correlation, indicating that the electron-donating groups increase and electron-withdrawing groups decrease electron density on the $Fe_3(CO)_9$ core. (Fig. 4) The energy spanned from the most electron-donating group (NMe_2) to the most electron-withdrawing group (CN) is approximately 20 cm^{-1}, almost half of the 45 cm^{-1} shift seen upon reduction of the neutral $Fe_3(CO)_9(\mu_3\text{-P}–p\text{-}C_6H_4X)(\mu_3\text{-P}–p\text{-}C_6H_4X')$ cluster to the monoanion. However, this large energy span is seen only for the CO stretching energies of the two most intense bands of the cluster series. The energy range spanned for the average energy of all three cluster CO stretching frequencies observed in THF (Tables 3, 6 and 8) is only 6 cm^{-1}. However, these energy values do show a linear, positive correlation with σ_p.

Fig. 4 also shows the Hammett correlation of the higher energy, intense CO band of the radical monoanion cluster series. It is of note that the correlation factor for this plot is as good as that of the neutral series and the energy spanned is the same. However, the energy span decreases dramatically to 3 cm^{-1} when the average of the energy of all observed CO stretches is correlated to the σ_p factors.

Plots of ν(CO) of the dianion cluster series versus σ_p also show the general expected trends. The correlation factor for this plot is in the same range as the neutral and monoanion, and the average correlates to the σ_p factors as well. The energy span decreases to approximately 5 cm^{-1} when the average is considered, as is expected from the neutral and monoanion cases.

2.3.2. Electron paramagnetic resonance data

The range of g values for the $Na[Fe_3(CO)_9(\mu_3\text{-P}–p\text{-}C_6H_4X)(\mu_3\text{-P}–p\text{-}C_6H_4X')]$ cluster series is small (Table 9), but a significant correlation with the Hammett parameter of the X substituent is observed (Fig. 5). This result is unexpected because no correlation is observed between the nature of the ligand and the g values in the monoanion radical cluster

Table 8
Infrared CO stretching frequencies (cm^{-1}) of $Na[Fe_3(CO)_9(\mu_3\text{-P}–p\text{-}C_6H_4X)_2]$ in THF solution

Cluster	ν(CO)1	ν(CO)2	ν(CO)3	ν(CO)4	ν(CO)5
[**2**–NMe_2:CN]$^-$	2028 (w)	1990 (vs)	1978 (s)	1951 (m)	1931 (m)
[**1**–NMe_2]$^-$	2026 (w)	1982 (vs)	1971 (s)	1961 (m)	1942 (m)
[**1**–OCH_3]$^-$	2027 (w)	1986 (vs)	1968 (s)	1960 (m)	1941 (m)
[**1**–CH_3]$^-$	2028 (w)	1988 (vs)	1976 (s)	1958 (m)	1942 (m)
[**1**–H]$^-$	2028 (w)	1990 (vs)	1977 (s)	1950 (m)	1935 (m)
[**1**–Cl]$^-$	2029 (w)	1992 (vs)	1980 (s)	1952 (m)	1935 (m)
[**1**–CF_3]$^-$	2031 (w)	1994 (vs)	1982 (s)	1953 (m)	1936 (m)
[**1**–CN]$^-$	2033 (w)	1997 (vs)	1984 (s)	1955 (m)	1938 (m)

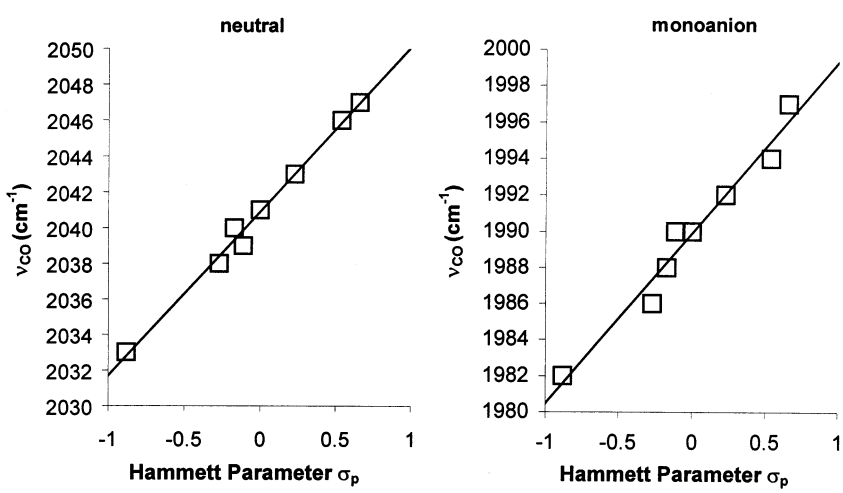

Fig. 4. Plot of ν(CO) for the neutral and monoanionic $Fe_3(CO)_9(\mu_3\text{-P}–p\text{-}C_6H_4X)_2$ clusters vs. Hammett parameter σ_p.

Table 9
EPR g values for the $Na[Fe_3(CO)_9(\mu_3\text{-}PC_6H_4X)(\mu_3\text{-}PC_6H_4X')]$ clusters [a]

Cluster	g Value
$[\mathbf{1}\text{–}NMe_2]^-$	2.02232
$[\mathbf{1}\text{–}OCH_3]^-$	2.02347
$[\mathbf{1}\text{–}CH_3]^-$	2.02346
$[\mathbf{2}\text{–}NMe_2\text{:}CN]^-$	2.02346
$[\mathbf{1}\text{–}H]^-$	2.02374
$[\mathbf{1}\text{–}Cl]^-$	2.02397
$[\mathbf{1}\text{–}CF_3]^-$	2.02417
$[\mathbf{1}\text{–}CN]^-$	2.02441

[a] The estimated error for these values is ± 0.00002. Measurements are taken at room temperature in THF as the Na^+ salt.

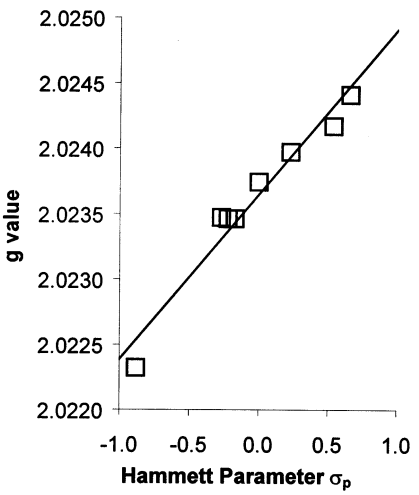

Fig. 5. Plot of g values vs. Hammett parameter σ_p.

series $Fe_3(CO)_8(L)_1(\mu_3\text{-}PC_6H_5)_2$ [8], or in studies of functionalized aromatic organic radicals. The lack of correlation in these molecules may be because the molecular orbital containing the unpaired electron changes too substantially upon functionalization to show linearity.

It appears the separation between the cluster surface and core allows a systematic change in the metal-based orbital occupied by the unpaired electron. A rigorous explanation for this phenomenon is not readily apparent, however the results can be qualitatively rationalized in terms of a shielding factor, similar to that used in ^1H NMR. As the electron density at the metal core is increased throughout the $Na[Fe_3(CO)_9(\mu_3\text{-}P\text{–}p\text{-}C_6H_4X)(\mu_3\text{-}P\text{–}p\text{-}C_6H_4X')]$ series, the energy necessary to induce the spin transition becomes higher, giving rise to a smaller g value, in accordance with the observed trend.

2.3.3. Electrochemistry data

The parent cluster, $Fe_3(CO)_9(\mu_3\text{-}PC_6H_5)_2$, and the functionalized clusters exhibit quasi-reversible electrochemical behavior and as a consequence of this feature shows a direct relationship between the observed $E_{1/2}$ and the natural logarithm of the rate of heterogeneous electron transfer, k_{et}. Theoretically, a LFER correlation can only be expected for an electrochemically irreversible series if the mechanism of heterogeneous electron transfer is the same for all members of the series [10]. Since the structures of the clusters are similar, it is assumed that the transfer coefficient, α, does not change significantly within the series. The degree of reversibility within the series, as determined quantitatively by the ratio of anodic peak height to the cathodic peak height, i_{pa}/i_{pc}, and the difference between the cathodic peak potential and the anodic peak potential, ΔE_p values, varies considerably. Despite this nonconformity, the $E_{1/2}$ values for the first and second reductions show an excellent linear correlation with the Hammett σ parameter (Fig. 6).

2.3.4. Fenske–Hall molecular orbital calculations

The orbital interactions that mediate the electronic communication between the substituent on the aryl ring

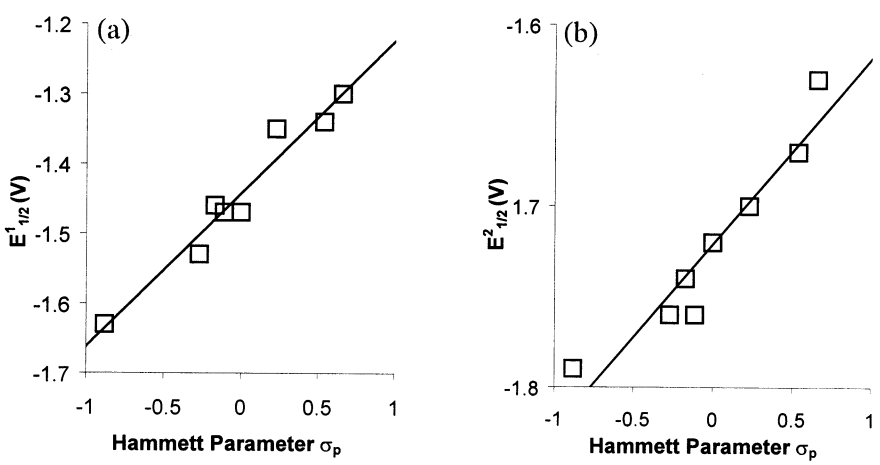

Fig. 6. Plot of $E^1_{1/2}$ vs. σ_p (a). Plot of $E^2_{1/2}$ vs. σ_p (b).

and the $Fe_3(CO)_9$ core were examined using Fenske–Hall molecular orbital calculations (see Section 4). The geometry of the $Fe_3(CO)_9(\mu_3\text{-}PC_6H_4X)_2$ cluster is taken from the crystal structure data and idealized to C_s symmetry.

The orbital picture for a disubstituted aromatic ring (in C_{2v} symmetry) is presented first to understand this fragment before examining its interaction with the $Fe_3(CO)_9$ core orbitals. The important valence molecular orbitals of the C_6H_4X fragment (X = Cl) are depicted in Fig. 7. The orbital with the lowest energy that we consider, $1b_1$, is an in-phase combination of the X-p_y atomic orbital and the π-system of the ring fragment. The second lowest orbital, $2b_1$, shows a significant X-p_y contribution (49%) and is clearly a π*-type interaction of the X atom with a π-orbital of the ring fragment. Orbitals $1a_2$ and $3b_1$ are derived from the highest filled orbitals of benzene (e_{1g}) and $2a_2$ and $4b_1$ are derived from the benzene π* orbitals of symmetry e_{2u}. Orbital $1a_1$ is a σ-bonding orbital oriented towards the phosphorus atom.

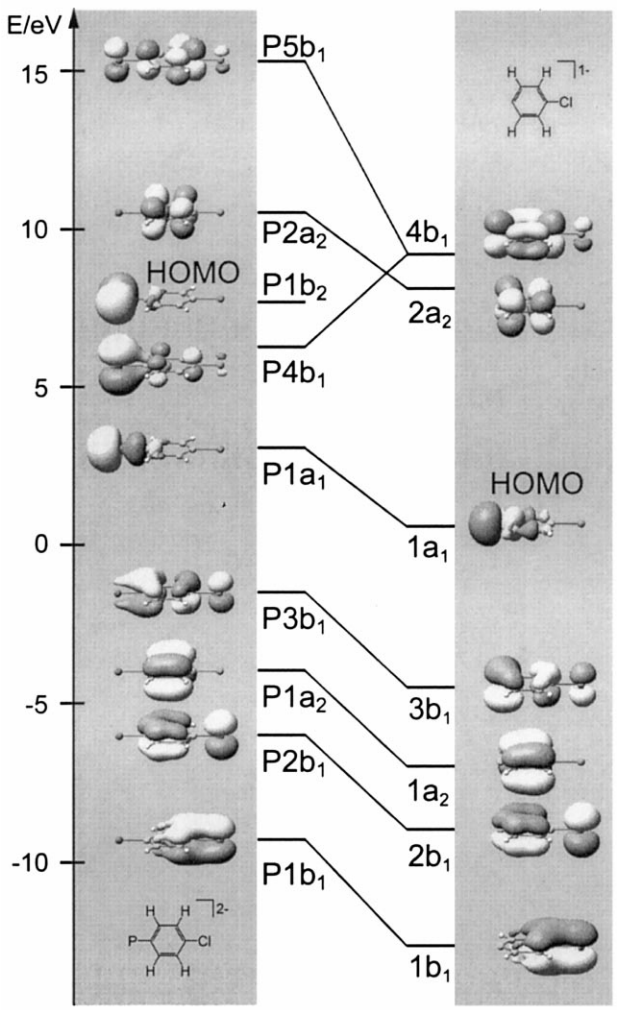

Fig. 7. Selected molecular orbitals of the $PC_6H_4Cl^{2-}$ (left) and $C_6H_4Cl^-$ (right) fragments.

The orbitals of the $P(C_6H_4X)$ fragment, shown on the left of Fig. 7, show that the interaction of the phosphorus p atomic orbitals with the ring fragment is weak. The three orbitals, $P1a_1$, $P4b_1$ and $P1b_2$, which are crucial for the interaction with the $Fe_3(CO)_9$ fragment, show no significant contributions from the X substituent. Only in $P4b_1$ is there a 2% contribution from the X-p_y orbital. Changes in the electronic nature of the X substituent are expected to be conveyed through the ring and affect the phosphorus atom in the *para* position. The main pathway for communication between the X-fragment and the phosphorus atom is through the molecular orbital $P4b_1$. This qualitative picture does not change with variations in the X group.

The Mulliken population of the phosphorus p_y atomic orbital shows a linear correlation with the Hammett σ_p parameter of X (Table 10 and Fig. 8), demonstrating the role of the X group in dictating the electronic characteristics of the phosphorus ligand. The systematic change in the P-p_y Mulliken population with different X groups is dictated primarily by the molecular orbital $P4b_1$. As X is varied from the electron-donating $N(CH_3)_2$ group to the electron-withdrawing CN group, there is a decrease in the population of the

Table 10
Mulliken population of the phosphorus atomic orbitals in the P–Ph–X fragment

X	p_x	p_y	p_z	s
NMe_2	1.986	1.691	1.257	1.663
OCH_3	1.986	1.671	1.255	1.662
CH_3	1.986	1.615	1.265	1.665
H	1.986	1.595	1.272	1.668
Cl	1.986	1.625	1.259	1.663
CF_3	1.986	1.544	1.272	1.667
CN	1.986	1.445	1.272	1.669

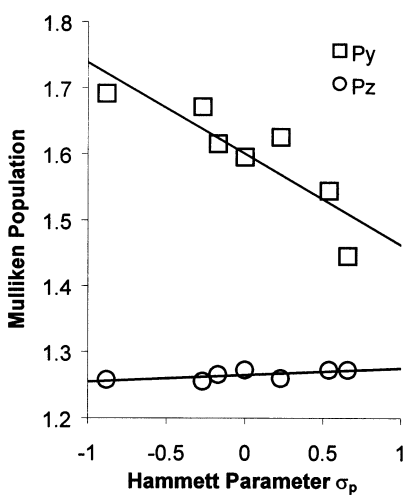

Fig. 8. Graph of the Mulliken population of phosphorus p_z and p_y orbitals vs. Hammett σ_p parameter.

phosphorus p_y orbital. This trend is in agreement with the expectation that the energy of the $4b_1$ orbital is lower for the electron-withdrawing substituent, thereby allowing a better overlap with the p_y atomic orbital, and resulting in a smaller Mulliken population. The HOMO of the $PC_6H_4Cl^{2-}$ fragment consists of 95.3% of phosphorus p_x orbital, which is parallel to the ring, and no significant contribution from the ring. Accordingly, no significant changes in Mulliken population are seen for the phosphorus p_x orbital. The p_z orbital population shows small changes, resulting from the weak σ-type interaction with the ring illustrated in Fig. 7.

Bonding between the phosphorus atom and $Fe_3(CO)_9$ core is primarily through the $Fe_3(CO)_9$ core 'e_g-type' d-orbitals of the iron atoms and the phosphorus p orbitals [11]. The overlap populations show that the bonding interactions between Fe_3 and the PR capping group is predominantly through π interactions with the p_x and p_y orbitals, with smaller contributions from σ-bonding with the p_z orbitals (Table 11). As a result of the low symmetry of the molecule, a complex pattern of orbital mixing is observed. However, there are only a few molecular orbitals with significant ($>5\%$) contributions from the phosphorus p orbitals. As expected, the interaction of the phosphorus p_z orbital with the metal center is σ in character, and does not show any significant change over the studied series of molecules. Molecular orbitals containing notable phosphorus p_x and p_y character are presented in Fig. 9. Fig. 9(a) and (b) show bonding and anti-bonding combinations of the two phosphorus p_x orbitals and suggest that the interaction of the p_x orbital with the iron core is electronically insensitive to variations of the X fragment. The π-orbitals depicted in Fig. 9(a) and (b) show 0.4 and 2.5% contributions from the chlorine-based p_x orbital, respectively.

Table 11
Overlap population between P and the Fe_3 core

	Phosphorus orbitals				Total
	p_x	p_y	p_z	s	
Fe_3(d, s, p)	0.323	0.429	0.073	0.035	0.861
Fe(1)	0.247	0.012	0.025	0.009	0.292
Fe(2)	0.036	0.209	0.021	0.044	0.281
Fe(3)	0.040	0.207	0.028	0.012	0.288

There are four occupied molecular orbitals with large phosphorus p_y and iron d orbital character. Fig. 9(c) shows a low lying π-interaction that propagates throughout the molecule. In Fig. 9(c), the phosphorus p_y orbitals are in-phase across the metal center; the out-of-phase combination is 1.6 eV higher in energy. Fig. 9(d) illustrates one of two nearly energetically degenerate molecular orbitals that are mostly derived from the phosphorus p_y orbital. These molecular orbitals are well suited for electronic communication through the ring as indicated by the delocalized shape of the orbital.

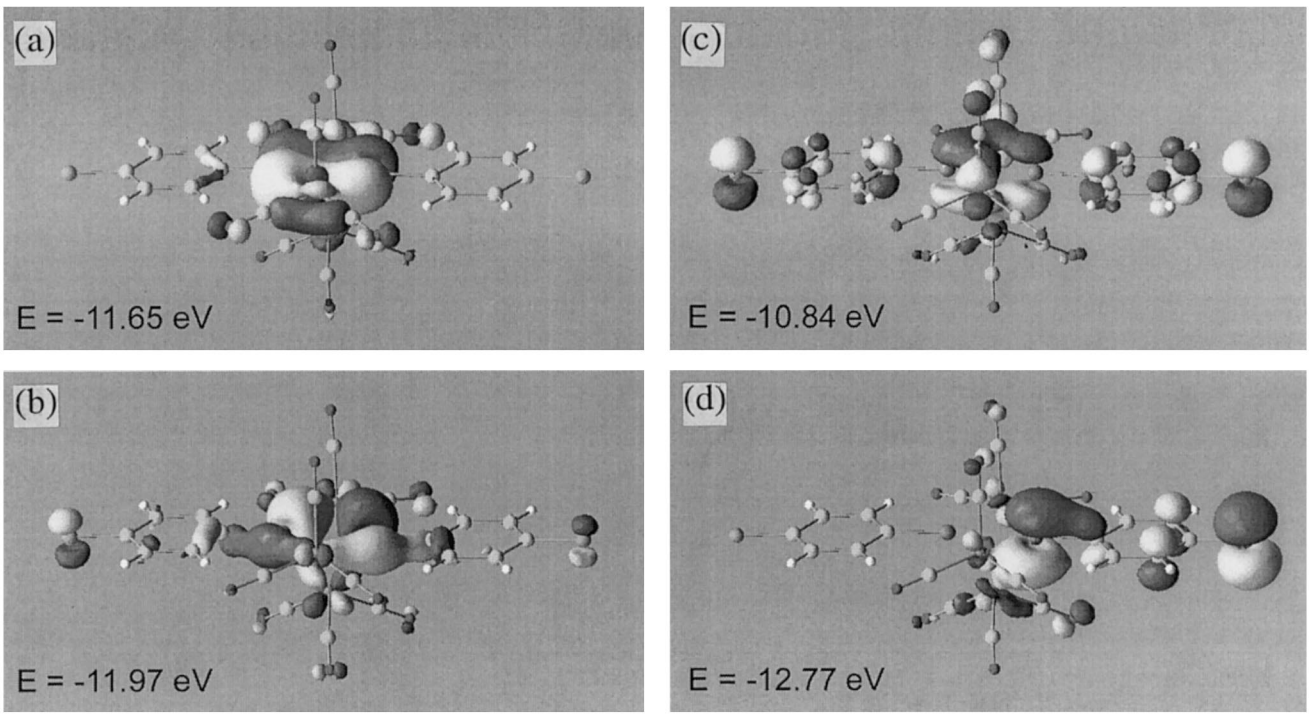

Fig. 9. π-Type interactions of the $Fe_3(CO)_9$ core with the phosphorus p_x and p_y orbitals.

Table 12
Mulliken population of the phosphorus atomic orbitals in the $Fe_3(CO)_9(\mu_3\text{-P}\text{–}p\text{-}C_6H_4X)_2$ cluster

Cluster	p_x	p_y	p_z	s
[**1**–NMe_2]	1.183	1.178	0.931	1.514
[**1**–OCH_3]	1.178	1.171	0.924	1.513
[**1**–CH_3]	1.183	1.178	0.931	1.514
[**1**–H]	1.187	1.184	0.939	1.515
[**1**–Cl]	1.182	1.177	0.929	1.513
[**1**–CF_3]	1.190	1.189	0.940	1.515
[**1**–CN]	1.191	1.184	0.936	1.515

Unlike for the $p\text{-}XC_6H_4P$ fragments, the Mulliken population of the phosphorus p_x and p_y orbitals in the cluster series do not display any systematic correlation with X (Table 12). The infrared CO stretching frequency is a sensitive probe of the electron density at the metal, and the observed systematic trend for this series of clusters (Table 3) is an empirical measure of the direct relationship between the electron density at the metal center and the X substituent of the aromatic cap. Although the orbital pathways for communication of the remote X substituent to the cluster core can be identified, the approximate nature of the Fenske–Hall method apparently does not allow a detailed investigation of the absolute orbital energy changes that result from the relatively minor perturbation of the overall electronic structure by X.

3. Conclusion

The influence of changes in the X substituent bound to the aromatic ring on the cluster properties in the series, $[Fe_3(CO)_9(\mu_3\text{-P}\text{–}p\text{-}C_6H_4X)_2]^{0/-1/-2}$, have been examined by a number of techniques. The structural characterizations for two neutral derivatives indicate that there are no significant changes in the cluster structural parameters as a function of X. A systematic tuning of the electronic structure of the derivatized clusters by X is indicated by linear correlations of the Hammett σ_p parameter with infrared CO stretching frequencies (for the neutral, monoanion, and dianion), redox potentials, and EPR g values (of the radical monoanion). The range in redox potential values observed between the most electron-donating and electron-withdrawing cluster examined are comparable to changes resulting from ligand substitution directly at the Fe_3 core. Fenske–Hall molecular orbital calculations allow the orbital pathways for communicating the effect of the X substituent to the cluster core to be identified, but no quantitative correlations are observed for the derivatized clusters.

4. Experimental

4.1. General procedures and materials

Unless otherwise noted, all manipulations were performed under an atmosphere of pre-purified nitrogen using standard Schlenk and glove-box techniques. The reagents PCl_3 (Johnson Matthey) and $Fe(CO)_5$ (Strem) were degassed by the freeze-pump-thaw method and vapor distilled immediately before use. Reagent grade tetrahydrofuran, diethyl ether, and benzene were freshly distilled from sodium benzophenone ketyl. Reagent grade ethyl acetate was purified by standard methods [12] and freshly distilled from P_2O_5. Reagent grade petroleum ether was purified and freshly distilled from $CaCl_2$. Column chromatography was performed under nitrogen at medium pressure with 60–200 mesh silica gel (Baker) or 100–200 mesh florisil (Chemical Dynamics). All other reagents are used as obtained without further purification. Tetrabutylammonium hexafluorophosphate (Aldrich) was recrystallized from ethyl acetate/pentane and dried under a dynamic vacuum for eight hours at 60°C. All spectroscopic and electrochemical measurements were carried out in the same solvent, tetrahydrofuran, for consistency. ^1H NMR spectra were recorded in CD_2Cl_2, which was freeze-pump-thaw degassed and vapor distilled from P_2O_5 immediately before use.

4.2. Spectroscopic measurements

Infrared spectra were recorded on a Bomem Michelson 120 FTIR spectrometer as THF solutions in a CaF_2 windowed cell.

UV–Vis spectra were recorded on a Hewlett–Packard 8452A diode-array spectrophotometer in CH_3CN solution.

^1H NMR data were acquired on a Bruker AC 200 at 200.132 MHz in CD_2Cl_2 solution; the resonance for residual $CHDCl_2$ ($\delta = 5.32$ ppm) served as the reference peak. The $^{31}P\{^1H\}$ NMR data were acquired on Bruker WM 250 (at 101.270 MHz) or Bruker AC 200 (at 81.015 MHz) spectrometers. The resonance for $P(OMe)_3$ ($\delta = 140$ ppm) contained in a concentric tube served as a reference signal.

EPR spectra were taken at room temperature on a Jeol Jesreix ESR spectrometer using an X band microwave bridge. Radical samples were prepared by the Na/Hg amalgam reduction procedure in tetrahydrofuran solution (see below) and experiments were conducted on sample in 1 mm quartz tubes. The sweep width, field center, field modulation, time constant and scan time were held constant for all experiments. The microwave frequency was measured by a HP 5340 A

frequency counter and DPPH ($g = 2.00370$) was used to standardize the magnetic field. The g values, thus determined, are accurate to ± 0.00002. The hyperfine coupling constants, $< a >_p$, were obtained by taking the difference of the peak-to-peak field separation directly from the EPR spectra. All $< a >_p$ values are reported in Gauss.

4.3. Electrochemical measurements

Cyclic voltammetry experiments were conducted using a Princeton applied research potentiostat/galvanostat model 273 equipped with a Yokogawa 3025 XY recorder using positive feedback IR compensation. Cyclic voltammograms were obtained in a single-compartment air-tight three-electrode cell under nitrogen on THF solutions 0.001 M in cluster and 0.1 M in tetrabutylammonium hexafluorophosphate. A platinum working electrode, a platinum spiral counter electrode and a silver wire quasi-reference electrode were used. The scan rates for each cluster were varied from 25 to 1000 mV s^{-1}. As the scan rate increases, the waves broadened considerably, indicating a slow rate of heterogeneous electron transfer. The plot of the square root of scan rate ($v^{1/2}$) with $\Delta E_{1/2}$ is linear, indicating the electrochemical irreversibility of this system [13]. The reported $E_{1/2}$ values are the average of the E_{pc} and E_{pa} for each wave, and the potentials are reported relative to ferrocene (0.0 V). The ΔE_p are standardized to those of an internal ferrocene standard. The i_{pa}/i_{pc} ratios were determined by the method of Adams [14].

4.4. Calculations

The molecular orbital calculations were performed on a Silicon Graphics Indigo2 workstation using the Fenske–Hall molecular orbital calculation package [15]. In all calculations the local coordinate system of the phenyl ring carbons was oriented with the x-axis perpendicular to the plane of the ring and z-axis parallel to a line between the two phosphorus atoms (or with the y-axis pointing into the ring). The structure used for the calculations was idealized to C_s symmetry from the crystal structure data reported for the **1**–H, **2**–NMe_2:CN, and **1**–NMe_2 clusters. The phenyl ring was rotated about the P–P axis so that it was parallel to the open edge of the cluster and the carbonyls on the apical iron were rotated slightly, placing the mirror plane in the P–Fe–P plane. The phenyl-X distances were estimated using typical values.

4.5. X-ray structure determinations

The structures were solved using software from the NRCVAX computing package [16]. Least-squares refinement on F minimized the function $\Sigma w(|F_o| - |F_c|)^2$. Crystals of **1**–$NMe_2$ suitable for X-ray analysis were obtained by slow diffusion of hexanes into a saturated benzene solution of the cluster. Crystals of **2**–NMe_2:CN suitable for X-ray analysis were obtained by slow diffusion of hexanes into a saturated benzene solution of the cluster. The crystallographic parameters and computations are summarized in Table 13.

Table 13
Crystallographic experiments and computations for $Fe_3(CO)_9(\mu_3\text{-P–}p\text{-}C_6H_4NMe_2)_2\cdot C_6H_6$ (**2**–N(Me)$_2$·C_6H_6) and $Fe_3(CO)_9(\mu_3\text{-P–}p\text{-}C_6H_4NMe_2)(\mu_3\text{-P–}p\text{-}C_6H_4CN)\cdot C_6H_6$ (**1**–N(Me)$_2$:CN)·C_6H_6

Compound	**2**–N(Me)$_2$	**1**–N(Me)$_2$:CN·C_6H_6
Empirical formula	$C_{25}H_{20}Fe_3N_2O_9P_2$	$C_{30}H_{20}Fe_3N_2O_9P_2$
Formula weight	721.92	781.98
Temperature (°C)	−150	room temperature
Crystal system	Triclinic	triclinic
Space group	$P\bar{1}$	$P\bar{1}$
a (Å)	9.226(2)	9.286(3)
b (Å)	13.624(3)	13.825(4)
c (Å)	11.597(3)	26.175(4)
α (°)	91.70(2)	77.22(2)
β (°)	98.76(2)	82.91(2)
γ (°)	97.70(2)	88.74(3)
V (Å^3)	1425.7(6)	3252(1)
Z	2	4
$F(000)$	730.51	1581.06
D_{calc} (g cm^{-3})	1.68	1.60
Crystal size (mm)	$0.35 \times 0.25 \times 0.10$	$0.30 \times 0.30 \times 0.25$
Diffractometer	Rigaku AFC6S	Rigaku AFC6S
Radiation Mo Kα (Å)	$\lambda = 0.71073$	$\lambda = 0.\ 71073$
μ (Mo Kα) (cm^{-1})	16.7	14.7
Scan type	θ–2θ	θ–2θ
2θ Range (°)	50.0	45.0
Indices collected	$\pm h, +k, \pm l$	$\pm h, +k, \pm l$
Reflections ($I = 2.5\sigma(I)$)	3717	8542
	2164	6444
No. of least-squares parameters	370	829
R [a]	0.059	0.061
wR [b]	0.073	0.075
Error in observation of unit weight	1.94	1.76
Largest shift/error, final cycle	0.135	0.085

[a] $R = (\Sigma \, ||F_o| - |F_c||)/\Sigma \, |F_o|$.
[b] $wR = [\Sigma \, w(|F_o| - |F_c|)^2/\Sigma \, w(F_o)^2]^{1/2}$; $w = [\sigma^2(F_o) = k(F_o)^2]^{-1}$.

5. Syntheses

The aryldichlorophosphines, (p-$NMe_2C_6H_4$)PCl_2 [17], (p-$OCH_3C_6H_4$)PCl_2 [18], (p-$CH_3C_6H_4$)PCl_2 [19], (p-ClC_6H_4)PCl_2 [20], (p-CNC_6H_4)PCl_2 [21], were prepared by literature procedures. The preparation of (p-$CF_3C_6H_4$)PCl_2 was carried out by reaction of

$(Et_2N)_2PCl$ [22] with the appropriate Grignard reagent, followed by treatment with HCl. The reagent $Na_2[Fe_2(CO)_8]$ was prepared by following a literature procedure [23].

5.1. Synthesis of 1–NMe_2

A solution of $(p\text{-}NMe_2C_6H_4)PCl_2$ (3.5 g, 15.5 mmol) in 100 ml of THF is added to a slurry of $Na_2Fe_2(CO)_8$ (6.0 g, 15.5 mmol) in 100 ml of THF over the course of 2 h under a slow flow of N_2. The deep brown mixture is stirred overnight at room temperature and then the solvent is removed under vacuum. The residue is extracted into 300 ml of hexanes and the solvent is removed under vacuum. The residue is loaded in 45 ml of hexanes/benzene (75:25) on silica gel (3 × 30 cm) and chromatographed. Elution with hexanes/benzene (75:25) yields one red band. The solvent is removed under vacuum and the residue is recrystallized from CH_2Cl_2/Et_2O or benzene/hexanes to yield purple crystals. Isolated yield: 2.6 g (45% based on $(p\text{-}NMe_2C_6H_4)PCl_2$). *Anal.* Calc. For $C_{23}H_{14}Fe_3N_2O_9P_2$: C, 41.60; H, 2.81; N, 3.88. Found: C, 41.44; H, 2.72; N, 4.04%.

5.2. Synthesis of 1–OCH_3

The cluster, **1**–OCH_3, is synthesized in an analogous manner to **1**–NMe_2 (see above). The residue is chromatographed on silica gel (3 × 30 cm) and eluted with hexanes/benzene (80:20). The first two yellow bands are discarded and the third red band collected. The solvent is removed under vacuum and the residue is recrystallized from hexanes. Isolated yield: 1.2 g (24% yield based on $(p\text{-}OCH_3C_6H_4)PCl_2$).

5.3. Synthesis of 1–CH_3

The cluster, **1**–CH_3, is synthesized in a manner analogous to **1**–NMe_2. The residue is chromatographed on silica gel (3 × 30 cm). Elution with benzene/hexanes (1:1) yields one red band. The solvent is removed under vacuum and the residue is recrystallized from hexanes. Isolated yield: 780 mg (17% based on $(p\text{-}CH_3C_6H_4)PCl_2$).

5.4. Synthesis of 1–Cl

The cluster, **1**–Cl, is synthesized in a manner analogous to **1**–NMe_2. The residue is chromatographed on silica gel (3 × 30 cm). Elution with hexanes yields one red band. The solvent is removed under vacuum and the residue is recrystallized from hexanes. Isolated yield: 345 mg (4% based on $(p\text{-}ClC_6H_4)PCl_2$). *Anal.* Calc. for $C_{21}H_{14}Cl_2Fe_3O_9P_2$: C, 35.80; H, 1.30. Found: C, 35.88; H, 1.37%.

5.5. Synthesis of 1–CF_3

The cluster, **1**–CF_3, is synthesized in a manner analogous to **1**–NMe_2. The residue is chromatographed on florisil (3 × 30 cm). Elution with hexanes yields a dark orange band. The solvent is removed under vacuum and the residue is recrystallized from hexanes. Isolated yield: 1.2 g (5% based on $(p\text{-}CF_3C_6H_4)PCl_2$). *Anal.* Calc. for $C_{23}H_{14}F_6Fe_3O_9P_2$: C, 35.79; H, 1.3. Found: C, 35.83; H, 1.4%.

5.6. Synthesis of 1–CN

The cluster, **1**–CN, is synthesized in a manner analogous to **1**–NMe_2. The residue is chromatographed on florisil (3 × 30 cm). Elution with benzene yields a red band. The solvent is removed under vacuum and the residue is recrystallized from benzene/hexanes. This cluster is insoluble in hexanes. Isolated yield: 580 mg (10% based on $(p\text{-}CNC_6H_4)PCl_2$). *Anal.* Calc. for $C_{23}H_{14}Fe_3N_2O_9P_2$: C, 41.93; H, 1.53; N, 4.25. Found: C, 42.01; H, 1.61; N, 4.41%.

5.7. Synthesis of 2–NMe_2:CN

To 10.9 g (28.6 mmol) of $Na_2Fe_2(CO)_8$ in 500 ml of THF, a mixture of $(p\text{-}CNC_6H_4)PCl_2$ (21.4 mmol, 4.4 g) and $(p\text{-}NMe_2C_6H_4)PCl_2$ (7.4 mmol, 1.6 g) in 100 ml of THF is added over the course of 30 min. After stirring overnight, the THF is removed under vacuum and the residue is extracted with 200 ml of warm benzene. The volume of the solution is reduced under vacuum to 40 ml, and chromatographed in two parts on a 20 × 3 cm florisil column. Elution with hexanes/benzene (9:1) produces the first red band, which is **1**–NMe_2. Elution with hexanes/benzene (7:3) yields a thick purple band, **2**–NMe_2:CN. The third band, **1**–CN, is eluted with benzene. **2**–NMe_2:CN is recrystallized from hexanes. Isolated yield: 630 mg (3% based on $(p\text{-}NMe_2C_6H_4)PCl_2$). *Anal.* Calc. for $C_{24}H_{20}Fe_3N_2O_9P_2$: C, 40.95; H, 2.02; N, 4.01. Found: C, 41.17; H, 1.97; N, 3.87%.

5.8. General procedure for a Na/Hg chemical reduction

A 0.01 M solution of cluster in THF is transferred via a stainless steel cannula to a 1% (w/w) Na/Hg amalgam. The solution is swirled until the color changes from red to green. The end point of reduction is determined by IR spectroscopy. The dianion is prepared by leaving the cluster over the amalgam for a longer period of time. Reduction of the dianion is accompanied by a color change from green of the monoanion to red–brown of the dianion.

5.9. General procedure for a sodium benzophenone ketyl reduction

A 0.01 M solution of neutral cluster in THF is treated dropwise with a saturated THF solution of sodium benzophenone. The progression of reduction is monitored qualitatively by color change and quantitatively by IR spectroscopy for both the monoanion and the dianion species.

6. Supplementary material

Tables of atomic coordinates, complete bond distances and angles, anisotropic thermal parameters and structure factors for $Fe_3(CO)_9[\mu_3\text{-P}-p\text{-}C_6H_4N(CH_3)_2]_2$ and $Fe_3(CO)_9[\mu_3\text{-P}-p\text{-}C_6H_4N(CH_3)_2][\mu_3\text{-P}-p\text{-}C_6H_4CN]$ are available on request from the authors.

Acknowledgements

Professor M.D.E. Forbes and his group are acknowledged for assistance with EPR measurements. Partial support for this research was provided by the National Science Foundation.

References

[1] (a) L.P. Hammett, J. Chem. Phys. 4 (1936) 613. (b) L.P. Hammett, J. Am. Chem. Soc. 59 (1937) 96.
[2] (a) Y. Koide, M.T. Bautista, P.S. White, C.K. Schauer, Inorg. Chem. 31 (1992) 3690. (b) M.T. Bautista, P.S. White, C.K.J. Schauer, Am. Chem. Soc. 116 (1994) 2143. (c) M.R. Jordan, P.S. White, C.K. Schauer, M.A. Mosley, J. Am. Chem. Soc. 117 (1995) 5403.
[3] (a) P.M. Triechel, W.K. Dean, W.M. Douglas, Inorg. Chem. 11 (1972) 1609. (b) H. Vahrenkamp, E.J. Wucherer, D. Wolters, Chem. Ber. 116 (1983) 1219.
[4] J.K. Kouba, E.L. Muetterties, M.R. Thompson, V.W. Day. Organometallics 2 (1983) 1065.
[5] S.L. Cook, J. Evans, L.R. Gray, M. Webster, J. Organomet. Chem. 236 (1982) 36.
[6] (a) M.T. Bautista, P.S. White, C.K. Schauer, J. Am. Chem. Soc. 113 (1991) 8963. (b) O. Stelzer, H. Sommer, S. Hietkamp, D.J. Brauer, G. Muller, C. Kruger, J. Organomet. Chem. 288 (1985) 35.
[7] (a) C.E. Strouse, L.F. Dahl, J. Am. Chem. Soc. 93 (1971) 6032. (b) P.A. Dawson, B.M. Peake, B.H. Robinson, J. Sirnpson, Inorg. Chem. 19 (1980) 465.
[8] (a) H.H. Ohst, J.K. Kochi, J. Am. Chem. Soc. 108 (1986) 2897. (b) H.H. Ohst, J.K. Kochi, Inorg. Chem. 25 (1986) 2066.
[9] B.E. Bursten, M.R. Green, Prog. Inorg. Chem. 36 (1988) 393.
[10] P. Zuman, Substituent Effects in Organic Polarography, Plenum, New York, 1967, pp. 5–22.
[11] P.T. Chesky, M.B. Hall, Inorg. Chem. 22 (1983) 1339–1374.
[12] A.J. Gordon, R.A. Ford, The Chemist's Companion: A Handbook of Practical Data, Techniques, and References, Wiley, New York, 1972.
[13] A.J. Bard, L.R. Faulkner, Electrochemical Methods, Ch. 6, Wiley, New York, 1980.
[14] R.N. Adams, Electrochemistry at Solid Electrodes, Marcel Dekker, New York, 1969.
[15] (a) M.B. Hall, R.F. Fenske, Inorg. Chem. 11 (1972) 768. (b) R.F. Fenske, Pure Appl. Chem. 27 (1971) 61.
[16] E.J. Gabe, Y. Le Page, J.-P. Charland, F.L. Lee, P.S. White, J. Appl. Crystallogr. 22 (1989) 384.
[17] M.P. Viout, J. Rech. CNRS 28 (1954) 15.
[18] J.A. Miles, M.T. Beeny, K.W. Ratts, J. Org. Chem. 40 (1975) 343.
[19] B. Buchner, L.B. Lockhardt, J. Am. Chem. Soc. 73 (1951) 755.
[20] D.D. Magnelli, G. Tesi, J.H. Lowe, E.W. McQuiston, Inorg. Chem. 5 (1966) 457.
[21] L.D. Quin, J.S. Humphries, J. Am. Chem. Soc. 83 (1961) 4124.
[22] P.G. Chantrell, C.A. Pearce, J. Appl. Chem. 14 (1964) 563.
[23] H. Strong, P.J. Krusic, J. San Filippo, Inorg. Synth. 24 (1983) 157.